IEEE Photonics Journal
An IEEE Photonics Society Publication

Open Access

Dynamic Three-Dimensional Surface Reconstruction Approach for Continuously Deformed Objects

Volume 13, Number 1, February 2021

Jianhua Wang
Yanxi Yang
Yuguo Zhou

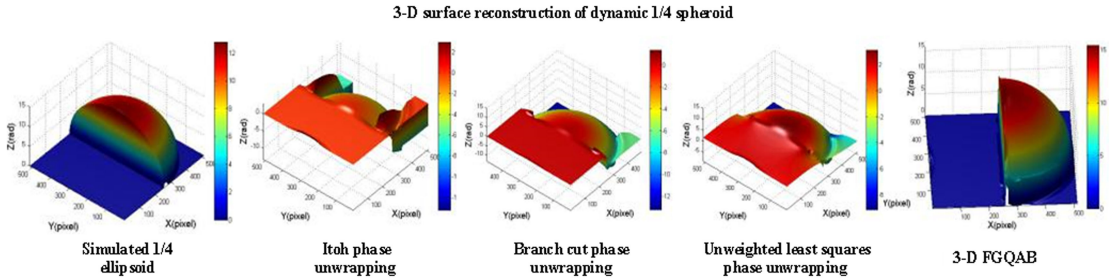

DOI: 10.1109/JPHOT.2021.3052932

Dynamic Three-Dimensional Surface Reconstruction Approach for Continuously Deformed Objects

Jianhua Wang,[1] **Yanxi Yang**,[2] **and Yuguo Zhou**[1]

[1]School of Information and Control Engineering, Qingdao University of Technology, Qingdao 266520, China
[2]Shaanxi Key Laboratory of Complex System Control and Intelligent Information Processing, Xi'an University of Technology, Xi'an 710048, China

DOI:10.1109/JPHOT.2021.3052932

Manuscript received November 15, 2020; revised December 27, 2020; accepted January 15, 2021. Date of publication January 22, 2021; date of current version February 3, 2021. This work was supported in part by the Shaanxi Key Laboratory of Complex System Control and Intelligent Information Processing (Contract No. 2020CP07), Xi'an University of Technology, and in part by the Key scientific research projects of colleges and universities in Shandong Province (Contract No. 2020VC12019). Corresponding author: Jianhua Wang (e-mail: wangjianhua@qut.edu.cn).

This article has supplementary downloadable material available at https://doi.org/10.1109/JPHOT.2021.3052932, provided by the authors.

Abstract: For dynamic three-dimensional (3-D) surface reconstruction of continuously deformed objects, an efficient method employing one fringe pattern is proposed. First, a two-dimensional wavelet transform profilometry (2-D WTP) employing an improved cost function is adopted to obtain the wrapped phase, which has the better noise suppression ability. Then, a new 3-D phase unwrapping algorithm is introduced to obtain the unwrapped phase, which includes four steps. a) A new 3-D residues recognition method is proposed. b) A 3-D branch cut construction algorithm based on an improved GA is proposed. c) A 3-D phase derivative variance quality map is established. d) A 3-D flood filling phase unwrapping algorithm guided by 3-D quality map avoiding 3-D branch cut (3-D FGQAB) is introduced to obtain the unwrapped phase. Simulation and experimental comparisons are carried out, the results show that the proposed method can be applied to dynamic 3-D reconstruction of the continuously deformed objects.

Index Terms: Dynamic 3-D surface, an improved cost function, 3-D phase unwrapping algorithm.

1. Instruction

Dynamic 3-D surface reconstruction of continuously deformed objects has wide application prospects. For example, when the object is subjected to impact, vibration or collision, real-time acquisition of the 3-D surface is beneficial to analyze product defects and improve product design. In the process of workpiece processing and manufacturing, real-time acquisition of the 3-D surface is helpful to optimize the processing parameters. In 3-D animation design, the fidelity of anime design can be improved by using the dynamic 3-D surface reconstruction of human facial expressions [1], [2].

Fringe projection profiometry (FPP) is one of the widely used 3-D surface reconstruction. Phase calculation of FPP is the key step, which generally includes two steps: wrapped phase

and unwrapped phase calculation. Wrapped phase calculation methods include phase-shifting profiometry (PSP) [3]–[6], Fourier transform profiometry (FTP) [7], and wavelet transform profiometry (WTP) [8]–[11]. PSP has high accuracy and strong anti-interference ability. It is insensitive to variation of ambient illumination and surface reflflectivity, thus becoming one of the most widely used 3-D surface reconstruction methods. However, it requires the measured object to be of constant surface and fixed position. Takeda *et al.* [7] proposed FTP. FTP only needs one fringe pattern to obtain the wrapped phase, so it can be used for the dynamic 3-D surface measurement of continuously deformed objects. However, noise, shadow and surface height jumps will cause spectrum aliasing and leakage, reducing the accuracy of FTP phase calculation. WTP only needs one fringe pattern to obtain the wrapped phase as well, it has the multi-resolution analysis ability. WTP makes up the defects of FTP and has better measurement accuracy than that of FTP. WTP uses one-dimensional wavelet transform (1-D WT) or two-dimensional wavelet transform (2-D WT) to calculate wrapped phase. 2-D WT not only has the scale factor, but also has the direction selectivity, therefore, 2-D WT is more suitable for fringe pattern analysis.

Since PSP, FTP and WTP use the arctangent function to extract phase, phase is wrapped into a range from $-\pi$ to π, which needs to be unwrapped. There are two categories of methods exist for phase unwrapping, temporal phase unwrapping and spatial phase unwrapping. Saldner and Huntley first proposed the temporal phase unwrapping method [12]. Later, some researchers proposed three pitches' unwrapping method, negative exponential unwrapping method and three pitches' heterodyne unwrapping method. The above methods project multiple sets of fringes with different frequencies along the time coordinate and unwraps the phase of each pixel individually. They have high accuracy and can be used to measure the objects with height jumps. However, they are not suitable for dynamic 3-D measurement of continuously deformed objects. Itoh first proposed spatial phase unwrapping method [13]. It only needs one wrapped phase to get the unwrapped phase. If we combine it with FTP or WTP, the dynamic 3-D measurement can be realized. However, it requires that the captured fringes satisfy the Nyquist sampling theorem. Due to the noise, shadow, or surface height jumps, however, this condition is difficult to meet, which gives rise to unwrapped phase errors. In addition, the phase errors propagate along the unwrapping path, which increase the errors. Although some path tracking algorithms (such as branch cut method, quality graph-oriented method, minimum cost flow method based on network planning, etc.) or path-independent global algorithms (such as weightless and weighted least squares, method based on Bayesian, etc.) have been proposed, but they can only limit the local errors to a smaller range.

Abdul-Rahman *et al.* [14] proposed a 3-D FTP, which can realize dynamic measurement of continuously changing objects. However, it still needs to be studied in terms of 3-D filter design and 3-D measurement of complex changing objects. Yee *et al.* [15] proposed a direct cosine function demodulation method based on color-coded sine fringes. The projected fringes are composed of red, green and blue based on the De Bruijn sequence. By matching with the De Bruijn sequence, the order of the fringes is directly identified from the colors of three consecutive fringes, thereby unwrapping the wrapped phase map into continuous phases. Then, it adopted the triangulation method to obtain the phase difference between the continuous phase map of the reference plane and the surface of the object, and reconstructed the 3-D surface. Flores *et al.* [16] proposed a 3-D measurement method for dynamic objects based on color fringe projection. Three sinusoidal phase shift fringe patterns based on the traditional three-step phase-shifting algorithm are integrated into the three channels of the color fringe pattern. Aiming at the information crosstalk between channels, a generalized phase shift algorithm is proposed.

Several composite phase shifting methods for absolute phase retrieval with less projected fringe patterns are developed. Liu *et al.* [17] presents a dual-frequency mode scheme, which can reduce the number of projected fringe patterns to six. That is, six fringe patterns can reconstruct a 3-D point cloud. Zuo *et al.* [18] proposed a bi-frequency tripolar pulse-width-modulation fringe projection method to reduce the number of fringe patterns. Therefore, $2 \times N$ (N-step phase shifting) fringe patterns are needed to reconstruct a 3-D shape. Zuo *et al.* [19] also proposed a method that employs four projection fringes to realize full-field phase unwrapping at a speed of 360 fps. In the

case of high-speed projection and capture, the above three methods try to reduce the number of fringe patterns to reconstruct a 3-D shape. However, due to the rapid changes on the objects surface, errors between multiple fringe patterns are inevitable.

For 3-D shape measurement of dynamically deformed objects, more than one fringe projection and capture usually bring errors. The reason is that when capturing multiple frames of fringe patterns, the object surface has changed. The method of calculating the phase information based on multiple fringes (such as the combination of phase-shifting method and multi-frequency method) inevitably will have large errors, even if high-speed projection and capture are used. In this work, we only need one fringe to calculate the wrapped phase and unwrapped phase with high precision, which avoids the frame-to-frame error when multiple fringe patterns are projected and captured. It is extremely challenging to calculate the phase with high accuracy based on a fringe. The main difficulty is that the Fourier transform method or wavelet transform method is susceptible to noise interference when calculating the wrapped phase, while the phase unwrapping is susceptible to interference from object height jumps and object shadows.

In addition, Zuo *et al.* [20] demonstrated a micro Fourier transform profilometry (μFTP), which can achieve acquisition rate up to 20000 fps. This method can recover a 3D point cloud with every two projected patterns. However, at very high projection and capture speed, the error between the two projected images can be approximately ignored. Fourier transform lacks the ability of local analysis. In the process of Fourier transform, spectrum aliasing and leakage will cause errors and affect its measurement accuracy. Two-dimensional wavelet transform profilometry based on the improved value function in this paper has good anti-noise ability and excellent time-frequency analysis characteristics, which makes up for the defects of Fourier transform.

The goal of this paper is to develop a new dynamic 3-D surface reconstruction method which can reconstruct 3-D surfaces robustly for continuously deformed objects. Its characteristics are as follows. First, only one fringe pattern is needed to reconstruct 3-D surface of the measured object. Therefore, there is no need to consider the problem of inter frame error when capturing multiple fringes. Second, an improved 2-D WT is introduced. Compared with the existing methods, the proposed algorithm has stronger noise suppression ability and higher phase calculation accuracy. Finally, a 3-D FGQAB (3-D flood filling phase unwrapping algorithm guided by 3-D quality map avoiding 3-D branch cut) is introduced to obtain the unwrapped phase. Compared with the two-dimensional phase unwrapping algorithm in a frame, the proposed 3-D phase unwrapping algorithm makes full use of the relationship between the phases of each frame. Therefore, there are more unwrapping paths and the unwrapped phase error is limited to a smaller range.

The remainder of this paper is organized as follows. 2-D WT employing an improved cost function is introduced in Section 2. In Section 3, a new 3-D spatial phase unwrapping method is presented. Simulation comparisons are carried out in Section 4. In Section 5, experimental results are given to verify the effectiveness of the proposed method. Section 6 summarizes this paper.

2. 2-D WTP Employing an Improved Cost Function

Principle of 2-D WTP is to find a scale factor and a rotate factor, to make the similarity between the wavelet and the signal can reach maximum, i.e., the modulus of two-dimensional wavelet transform coefficients can reach maximum. Therefore, we can extract the wrapped phase information by finding the maximum modulus of the 2-D WT, i.e., wavelet ridge. For example, the wavelet ridge of a row of pixels without noise interference is shown in Fig. 1(a). The wavelet ridge extraction method by finding the maximum modulus of two-dimensional wavelet transform coefficients has the advantages of simple and fast. While there is noise interference in the fringes, the maximum modulus of 2-D WT is not the real wavelet ridge, but the extreme point caused by noise interference. For example, the wavelet ridge of a row of pixels with noise interference is shown in Fig. 1(b). Wavelet ridge extraction method based on a cost function is proposed [21]–[26]. The principle is that the coefficient modulus which are produced by noise can be removed by wavelet ridge continuity.

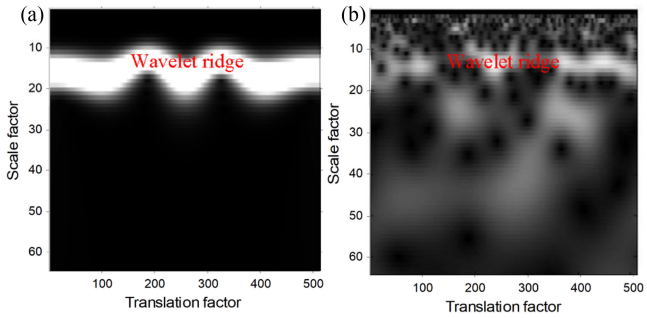

Fig. 1. Wavelet ridge of 2-D WT. (a) Noise free interference. (b) Noise interference.

The principle of 2-D WTP based on a cost function is that the extreme value of the 2-D WT coefficient module caused by noise can be removed by the continuity of the wavelet ridge, the cost function is expressed as

$$Cost[s(t), t] = -k_0 \int \left|m[s(t), t]\right|^2 dt + k_1 \int \left|\frac{\partial s(t)}{\partial t}\right|^2 dt, \tag{1}$$

where t represents the translation factor in x-axis, $s(t)$ is the scale factor, $m[s(t), t]$ is the modulus value at $[s(t), t]$, $\partial s(t)/\partial t$ represents the gradient of scale factor, k_0 and k_1 are two weighting coefficients.

Assume that $k_0 = 1$ and $k_1 = 1$, the discrete cost function can be presented as

$$\text{Cost}[s(t), t] = \sum_{b=2}^{W} \left\{-\left|m[s(t), t]\right|^2 + \left|s(t) - s(t-1)\right|^2\right\}, \tag{2}$$

where W represents the width of fringe pattern.

The last point of wavelet ridge goes through $[s(t), t]$, the cost function of subsequent point, $Cost$ $[s(t+1), t+1]$, can be expressed as

$$\text{Cost}\,[s(t+1), t+1] = \min\{\text{Cost}\,[s(t), t] - \left|m[s(t+1), t+1]\right|^2 + \left|s(t+1) - s(t)\right|^2\}. \tag{3}$$

The algorithm flow of 2-D WTP based on cost function is as follow. Firstly, all the extreme points are extracted from the modulus of two-dimensional wavelet transform coefficient, they constitute complete wavelet ridge candidates. Secondly, according to the principle that the large coefficient modulus caused by noise can be removed by wavelet ridge continuity, the gradient of scale factor is introduced into the modulus of the two-dimensional wavelet transform coefficient, then the cost function is established and used to evaluate the cost value of the whole candidate points. At last, the minimum cost value of candidates from the last pixel in each fringe line is selected, and the solution path of the minimum value of the candidate points is found to determine the optimal wavelet ridge in each fringe line.

However, the cost function takes the gradient of the scale factor into account, the direction information of fringe pattern is ignored. In this work, an improved cost function is proposed.

$$Icost[s(t), r(t), t] = -k_0 \int \left|m[s(t), r(t), t]\right|^2 dt + k_1 \int \left|\frac{\partial s(t)}{\partial t}\right|^2 dt + k_2 \int \left|\frac{\partial r(t)}{\partial t}\right|^2 dt, \tag{4}$$

where $r(t)$ is the rotate factor, $m[s(t), r(t), t]$ is the modulus value at $[s(t), r(t), t]$, $\partial s(t)/\partial t$ represents the gradient of scale factor, $\partial r(t)/\partial t$ represents the gradient of rotate factor, k_0, k_1 and k_2 are three weighting coefficients.

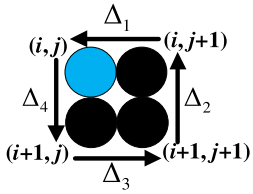

Fig. 2. Visualizing 2-D residue calculation for a 2-D point (*i, j*) in the wrapped phase.

Assume that $k_0 = 1$, $k_1 = 1$ and $k_2 = 1$, the discrete cost function can be presented as

$$Dlcost[s(t), r(t), t] = \sum_{b=2}^{W} \left\{ -\left|m[s(t), r(t), t]\right|^2 + \left|s(t) - s(t-1)\right|^2 + \left|r(t) - r(t-1)\right|^2 \right\}, \tag{5}$$

where *W* represents the width of fringe pattern.

Assume that *Dlcost* [(*s*(*t*), *r*(*t*), *t*)] is known, the discrete cost function of the subsequent wavelet ridge point, *Dlcost*[*s*(*t* + 1), *r*(*t* + 1), *t* + 1)], can be presented as

$$\begin{aligned} Dlcost\ [s(t+1), r(t+1), t+1] = \min Dlcost\{\ [s(t), r(t), t] - \left|m[s(t+1), r(t+1), t+1]\right|^2 \\ + \left|\Delta s(t)\right|^2 + \left|\Delta r(t)\right|^2\}, \end{aligned} \tag{6}$$

where $\Delta s(t) = s(t+1)$ - $s(t)$, $\Delta r(t) = r(t+1)$ - $r(t)$.

3. 3-D FGQAB

Traditional 2-D spatial phase unwrapping is applied to each frame of fringe pattern. For the dynamic 3-D surface measurement of continuous deformed objects, the method mentioned above does not consider the relationship between the fringe patterns of each frame. In this paper, we presented a 3-D flood filling phase unwrapping algorithm guided by 3-D quality map avoiding 3-D branch.

3.1 3-D Residue

Residues are defined to be local inconsistencies, which mark the beginning and end of 2π discontinuities. For a 2-D point (*i, j*) in the wrapped phase, the residues are identified when the value of '*k*' in (7) is 1 or –1 in a 2×2 closed path, otherwise $k = 0$, which indicates that no residue exists.

$$R(i,\ j) = \sum_{m=1}^{4} \Delta_m = 2\pi k \tag{7}$$

where Δ is shown in Fig. 2.

For a 3-D point (*i, j, t*) in the wrapped phase of *t*-th fringe pattern, the residue is identified by the following formula.

$$R^{ij} = \sum_{m=1}^{4} \Delta_m^{ij},\ R^{it} = \sum_{m=1}^{4} \Delta_m^{it},\ R^{jt} = \sum_{m=1}^{4} \Delta_m^{jt} \tag{8}$$

where Δ is shown in Fig. 3.

a) $R^{ij} = 0$ & $R^{it} = 0$ & $R^{jt} = 0$, 3-D points (*i, j, t*) is not a 3-D residue.
b) $NINT[R^{ij}/(2\pi)] = \pm 1$ & $R^{it} = 0$ & $R^{jt} = 0$, 3-D points (*i, j, t*) is a 3-D residue in *ij* plane, but it is not a 3-D residue in *it* plane and *jt* plane. We define it as local residue. The other two are similar.
c) $NINT[R^{ij}/(2\pi)] = \pm 1$ & $NINT[R^{it}/(2\pi)] = \pm 1$ & $NINT[R^{it}/(2\pi)] = \pm 1$, 3-D points (*i, j, t*) is a 3-D residue in all planes. We define it as global residue.

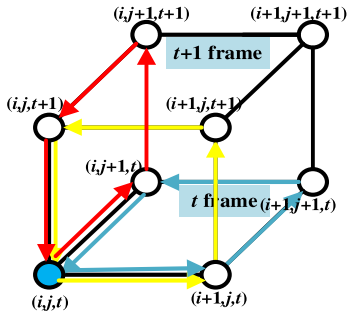

Fig. 3. Visualizing 3-D residue calculation for a 3-D point (*i*, *j*) in the wrapped phase of *t*-th fringe pattern.

3.2 3-D Spacial Branch Cut Construction Based on Improved Genetic Algorithm (GA)

a) If $NINT[R^{ij}/(2\pi)] = 1$, 3-D points (*i*, *j*, *t*) is defined as a positive 3-D residue. $NINT[R^{ij}/(2\pi)] = -1$, 3-D points (*i*, *j*, *t*) is defined as a negative 3-D residue. When the number of positive and negative residues is unequal, those with a small number of residues need to be supplemented to be equal. The supplementary residues can be used as positive residues or negative residues.

b) The positive 3-D residues are encoded into a positive chromosome sequence, and the negative chromosome sequence encoded by the negative 3-D residues is optimized. The fitness function is the sum of the Euclidean distance between all paired positive and negative residuals in the chromosome sequence.

$$fs = \sum_{i=1}^{N} \sqrt{[(x_i^+ - x_i^-)^2 + (y_i^+ - y_i^-)^2 + (z_i^+ - z_i^-)^2]}, \tag{9}$$

where *fs* is a fitness function, (x_i^+, y_i^+, z_i^+) is a index number of the *i*-th positive residue (local or global residue), (x_i^-, y_i^-, z_i^-) is a index number of the *i*-th negative residue (local or global residue).

c) Randomly generate chromosome sequences with negative residual points of different sorts, and use fitness function as the evaluation standard to pair positive and negative residues based on selection operator, crossover operator and mutation operator.

d) Spatial branch cut structure of paired 3D residues. It is worth noting that, for the 3-D residue in the local direction, the branch cut connected in the non-3-D residue direction are interrupted, and then the 3-D residue direction is reconnected according to the shortest path.

3.3 3-D Phase Derivative Variance Quality Map

As shown in Fig. 4, 3-D phase derivative variance at the pixel (*i*, *j*, *t*) in the *t*-th wrapped phase is defined as

$$\begin{aligned} Q(i,j,t) = & \frac{\sqrt{\sum_{m=i-k/2}^{i+k/2}\sum_{n=j-k/2}^{j+k/2}(\Delta^x(m,n,t) - \overline{\Delta^x(i,j,t)})^2}}{k^2} \\ & + \frac{\sqrt{\sum_{m=i-k/2}^{i+k/2}\sum_{n=j-k/2}^{i+k/2}(\Delta^y(m,n,t) - \overline{\Delta^y(i,j,t)})^2}}{k^2} \\ & + \frac{\sum_{m=i-k/2}^{i+k/2}\sum_{n=j-k/2}^{j+k/2}(\Delta^{t+}(m,n,t) - \overline{\Delta^{t+}(i,j,t)})^2}{k^2}, \end{aligned} \tag{10}$$

where *Q* represents the 3-D phase derivative variance at the pixel (*i*, *j*, *t*) in the *t*-th wrapped phase. The size of the neighborhood window is $k \times k \times 2$. In Fig. 4, $k = 3$. Δ_{mnt}^x and Δ_{mnt}^y represent the

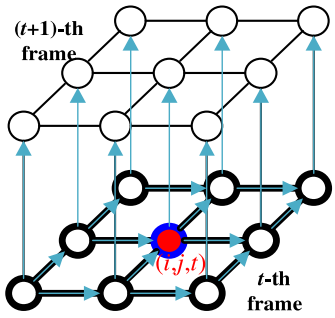

Fig. 4. 3-D phase derivative variance calculation at the pixel (*i*, *j*, *t*).

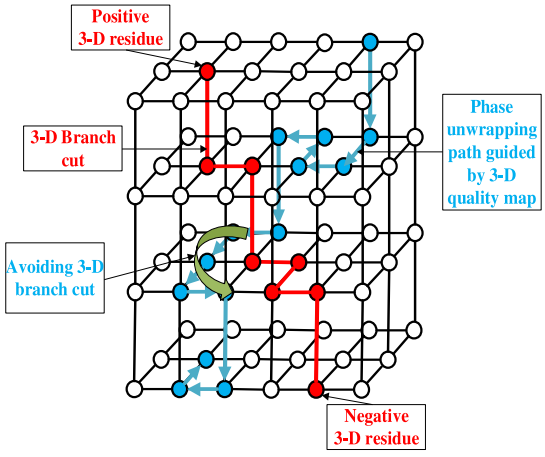

Fig. 5. 3-D flood filling phase unwrapping algorithm guided by 3-D quality map avoiding 3-D branch cut.

partial derivatives of pixels (*m*, *n*, *t*) in the *x* and *y* directions in the $k \times k$ neighborhood of (*i*, *j*, *t*). $\overline{\Delta^{x}_{ijt}}$ and $\overline{\Delta^{y}_{ijt}}$ represent the mean partial derivatives in the $k \times k$ neighborhood of (*i*, *j*, *t*). Δ^{t+}_{mnt} represents the difference between the phase of (*m*, *n*, $t+1$) and the phase of (*m*, *n*, *t*). $\overline{\Delta^{t+}_{ijt}}$ represents the mean difference between the phase of (*m*, *n*, $t+1$) and the phase of (*m*, *n*, *t*).

3.4 3-D FGQAB

As shown in Fig. 5. First, the algorithm selects a highest-quality phase point as the starting point for phase unwrapping. Subsequently, the algorithm selects the highest-quality phase point from the six adjacent phase points, and unwrapped it after avoiding the 3-D branch cut. The algorithm stores the neighboring pixels of the unwrapped pixel in "candidates". Finally, find the highest quality pixels from the "candidates" and perform phase unwrapping after avoiding the 4-D branch cut, and update their "candidates". The algorithm repeats the above steps until all pixels are expanded.

4. Simulation Comparison

4.1 Simulation Comparisons of the Wrapped Phase Calculation Accuracy

Two-dimensional Morlet mother wavelet is adopted in this work, which can be expressed as

$$\psi_M(x, y) = \exp\left(-\frac{1}{2}\sqrt{x^2 + y^2}\right) \times \exp\left[ik(x\cos\theta + y\sin\theta)\right], \tag{11}$$

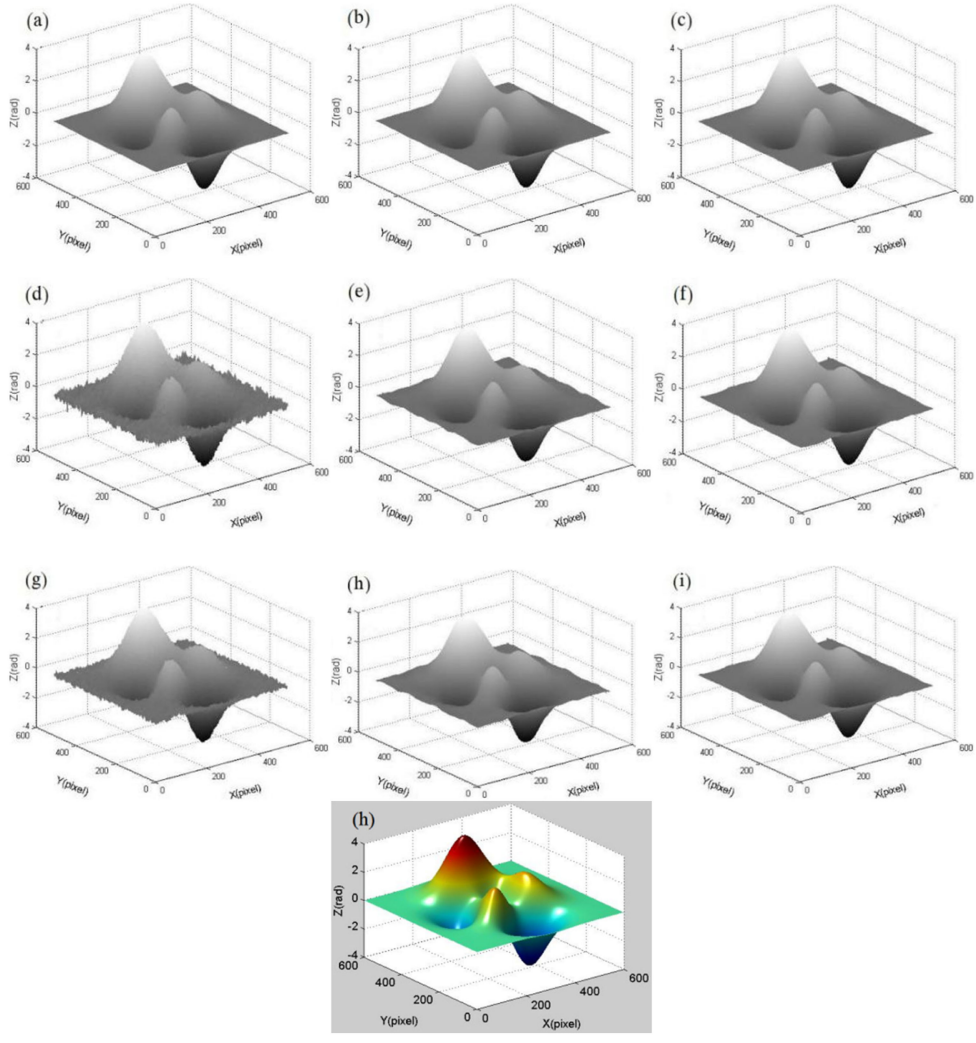

Fig. 6. Simulation comparisons of calculating wrapped phase. (a) WRE-DMM and Itoh (without noise). (b) WRE-ECF and Itoh (without noise). (c) WRE-ICF and Itoh (without noise). (d) WRE-DMM and Itoh (with 0.3 pepper & salt noise). (e) WRE-ECF and Itoh (with 0.3 pepper & salt noise). (f) WRE-ICF and Itoh (with 0.3 pepper & salt noise). (g) WRE-DMM and Itoh (with 0.5 Gaussian noise). (h) WRE-ECF and Itoh (with 0.5 Gaussian noise). (i) WRE-ICF and Itoh (with 0.5 Gaussian noise). (h) The simulated object 0.5 $\times$ Peaks.

where $i = \sqrt{-1}$, θ is the orientation angle with respect to the x-axis, and k is the frequency of the mother wavelet.

Two-dimensional wavelet transform of fringe pattern,

$$W(a, b, s, \theta) = \frac{1}{s^2} \int \int I(x, y) \psi_M \left(\frac{x - a}{s}, \frac{y - b}{s}, r_\theta \right) \mathrm{d}x\mathrm{d}y, \tag{12}$$

where a and b represents the translation factor in x-axis and y-axis, r represents the rotate factor, s represents the scale factor. In this work, $k = 5.336$, $\theta = \{0, \pi/6, \pi/3, \pi/2\}$, $s = \{1, 2, \ldots, 64\}$. The values of a and b are consistent with the image size.

The simulated object is 0.5 $\times$ *Peaks*, where Peaks is a function provided by Matlab. As shown in Fig. 6 (h). In order to compare the effectiveness of the proposed method, a standard deviation of 0.3

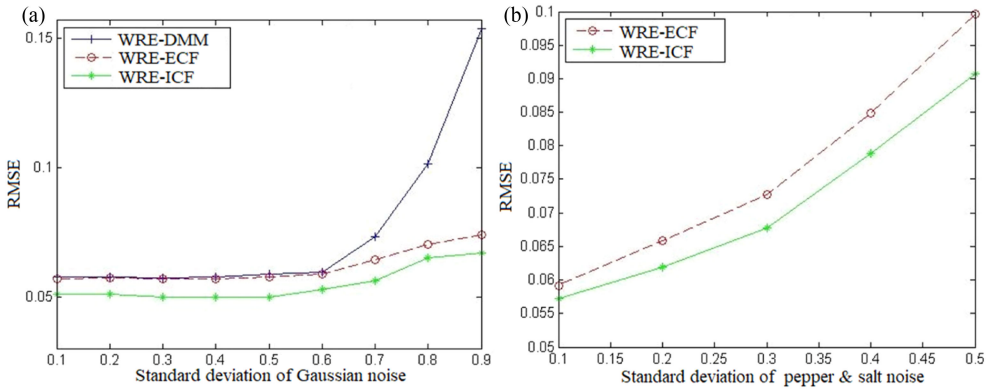

Fig. 7. RMSEs comparisons. (a) Gaussion noise. (b) Salt & pepper noise (amplification).

pepper & salt noise and a standard deviation of 0.5 Gaussian noise are added to the simulated objects. Wavelet ridge extraction algorithm based on direct maximum modulus (WRE-DMM), wavelet ridge extraction algorithm based on the exist cost function (WRE-ECF) and wavelet ridge extraction algorithm based on the improved cost function (WRE-ICF) are used to obtain the wrapped phase, respectively. The unwrapped phase is calculated by Itoh's phase unwrapping method [13]. The reconstructed 3-D surfaces are shown in Fig. 6. It can be seen from the simulation comparisons that WRE-DMM has obvious 3-D surface errors, and WRE-ECF can greatly suppress the interference of noise on the wavelet ridge extraction, but there are still some small folds. Reconstructed 3-D surfaces based on WRE-ICF are better than that of other methods.

In order to further verify the effectiveness of the proposed method, salt & pepper noise and Gaussian noise with a standard deviation gradient of 0.1 are added in sequence, and the measurement errors are calculated using root mean square error (RMSE).

RMSE can be expressed as

$$RMSE = \sqrt{\frac{\sum_{j=0}^{N-1}\sum_{i=0}^{M-1}\left(\phi_O(i,\,j)-\phi_R(i,\,j)\right)^2}{MN}}, \tag{13}$$

where $\varphi_{\mathrm{O}}(x,\,y)$ represents the original phase information, $\varphi_R(x,\,y)$ represents the real phase information, and M and N are the number of pixels in the x-axis and y-axis, respectively.

It can be seen from Fig. 7 that when the standard deviation is small, RMSEs are close, however, when the standard deviation increases, RMSES based on WRE-ICF are smaller than that of WRE-ECF and much smaller than that of WRE-DMM.

4.2 Simulation Comparisons of Unwrapped Phase Calculation Accuracy

Computer simulation of increasing 1/2 or 1/4 ellipsoid can be expressed as

$$\phi(x,\,y,\,t) = 0.001 \times k(t) \times \sqrt{65536-(x-256)^2-(y-256)^2}, \tag{14}$$

where $k(t)$ represents the height coefficient, which increases with time t. It is used to simulate an object that increases continuously with time. When $x\epsilon[1,\,512]$ and $y\epsilon[1,\,512]$, it is a 1/ 2 Ellipsoid. When $x\epsilon[257,\,512]$ and $y\epsilon[1,\,512]$, it is a 1/4 ellipsoid.

The wrapped phase is calculated by WRE-ICF. In the case that the wrapped phase is exactly the same, we compare the unwrapped phase using different phase unwrapping algorithms. Itoh phase unwrapping [13], branch cut phase unwrapping [27], [28], unweighted least squares phase unwrapping [29] and the 3-D FGQAB proposed in this paper are adopted and compared, respectively. Dynamic 3-D surface measurement results of the continuously changing 1/2 ellipsoid and 1/4

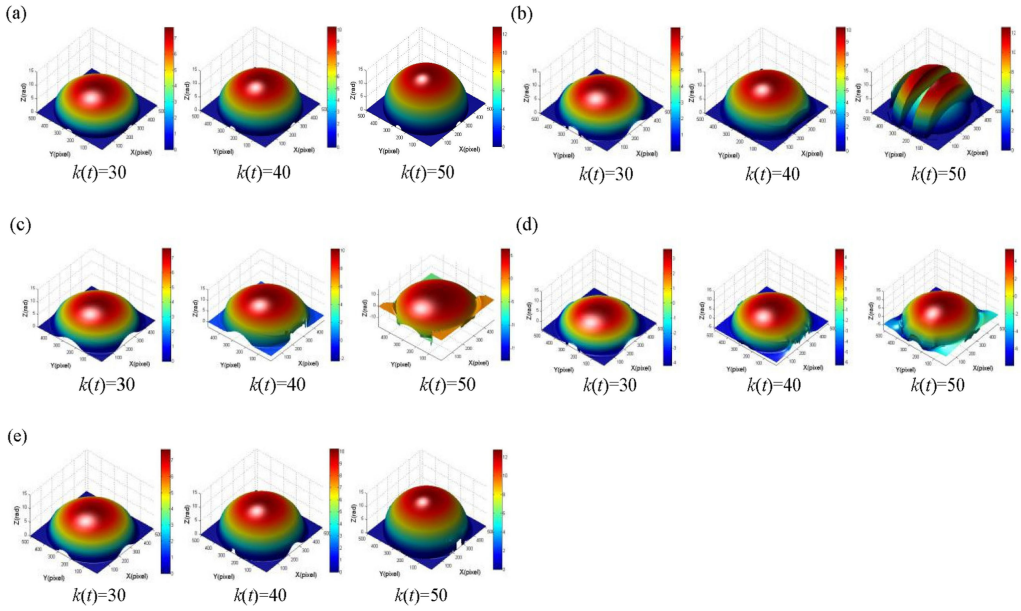

Fig. 8. 3-D surface reconstruction of dynamic 1/2 spheroid. (a) Simulated 1/2 ellipsoid (Video 1). (b) Itoh phase unwrapping. (c) Branch cut phase unwrapping (Video 2). (d) Unweighted least squares phase unwrapping. (e) 3-D FGQAB (Video 3).

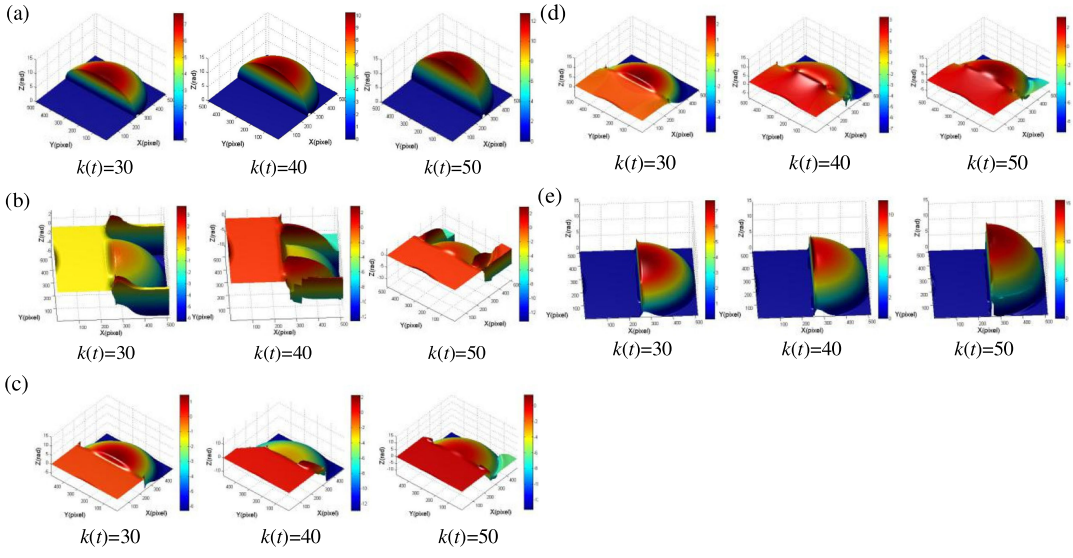

Fig. 9. 3-D surface reconstruction of dynamic 1/4 spheroid. (a) Simulated 1/4 ellipsoid. (b) Itoh phase unwrapping. (c) Branch cut phase unwrapping. (d) Unweighted least squares phase unwrapping. (e) 3-D FGQAB.

ellipsoid are shown in Figs. 8 and 9. It can be seen that the 3-D FGQAB proposed in this work can correctly reconstruct the 3-D surfaces of the objects when the objects' surfaces are discontinuous.

When the height coefficient $k\ (t) = 50$, the reconstructed 3-D surfaces of 1/2 ellipsoid and 1/4 ellipsoid are shown in Fig. 10. It can be seen from the comparisons that when the height of the object surfaces change greatly, Itoh phase unwrapping generates errors, meanwhile, the phase errors will be accumulated along the unwrapping direction, and an obvious pulling line phenomenon occurs. Reconstructed 3-D surfaces based on branch cut phase unwrapping has a

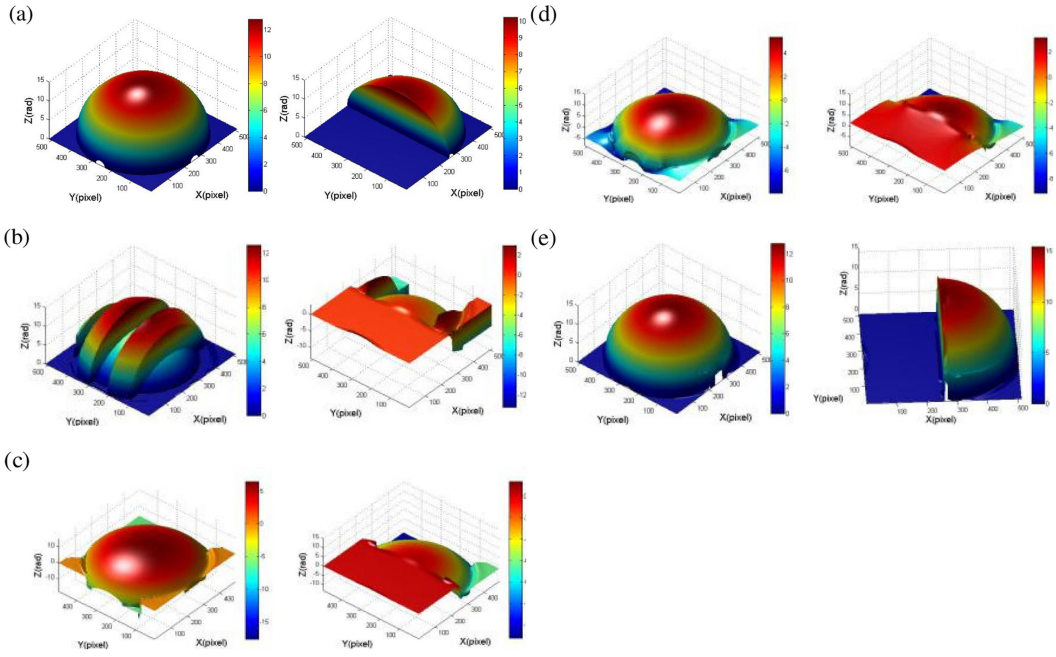

Fig. 10. 3-D reconstructed surfaces comparisons of $k(t) = 50$. (a) Simulated ellipsoids. (b) Itoh phase unwrapping. (c) Branch cut phase unwrapping. (d) Unweighted least squares phase unwrapping. (e) 3-D FGQAB.

TABLE 1
RMSEs Comparisons

Simulated object	Itoh phase unwrapping	Branch cut phase unwrapping	Unweighted least squares	3-D FGQAB
1/2 ellipsoid	4.0897	4.0510	6.8699	0.2039
1/4 ellipsoid	7.6299	5.5466	6.1401	0.4923

good consistency with the measured objects, and only generates errors in local areas where noise, shadows and heights change drastically. However, when there are many residues on residues map, the branch cut lines are dense and easy to produce islands, the phase unwrapping errors will be significantly increased. Although the overall 3-D surfaces based on the least square method seem to be better, in reality, the 3-D surface distortion will occur. This is because the method is a global algorithm, which uses the minimum global error as the optimization criterion, but will sacrifice the consistency of the reconstructed surface and the measured object. The 3-D surfaces reconstructed by the 3-D FGQAB proposed in this work are obviously superior to the 3-D surfaces reconstructed by the other methods.

In order to achieve quantitative comparisons, the 3-D measurement errors are evaluated by RMSE. The results are shown in Table 1. It can be seen that the RMSEs of the 3-D FGQAB is much smaller than that of the other three methods.

5. Experimental Comparison

3-D measurement system consists of a digital light processing projector (DLP LightCrafter 4500), a CCD camera (MER-050-560U3M), Single-Chip Microcomputer and a personal computer with Intel Core i5-4258U CPU, as is shown in Fig. 11.

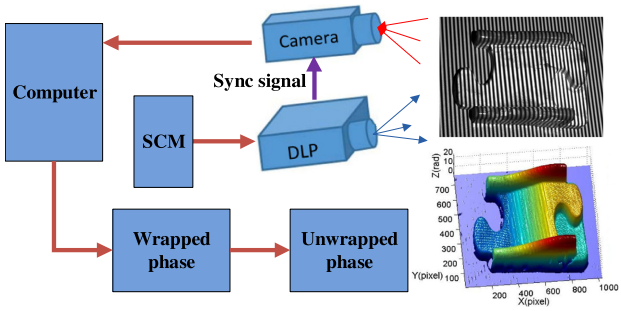

Fig. 11. 3-D measurement system.

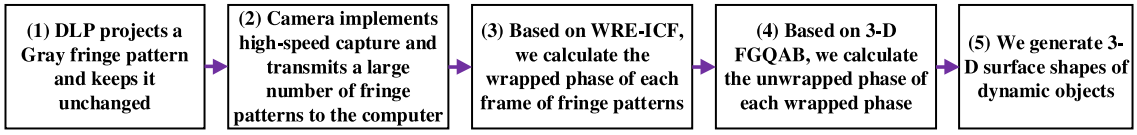

Fig. 12. Flowchart of the experimental process.

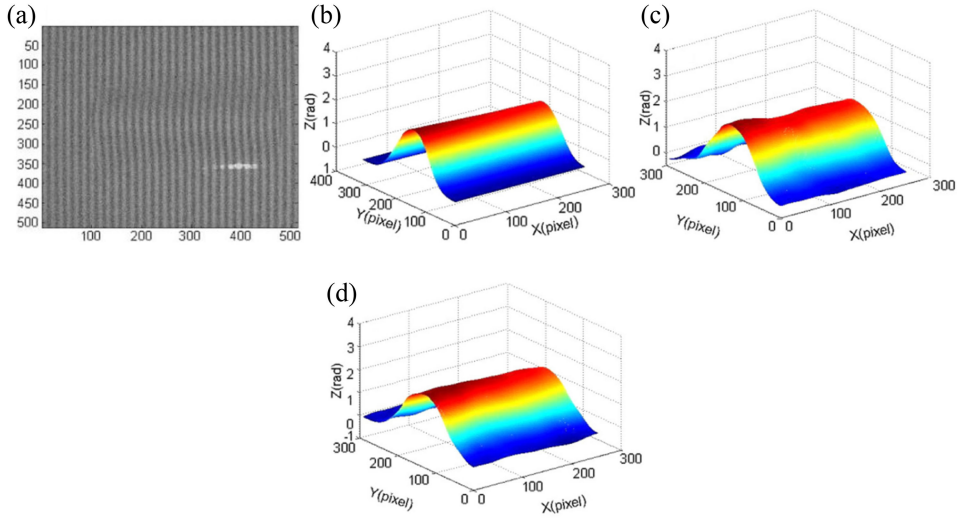

Fig. 13. Experimental comparisons of the wrapped phase calculation accuracy. (a) Noisy fringe. (b) Phase-shifting method. (c) WRE-ECF and Itoh. (d) WRE-ICF and Itoh.

The projection fringe is stored in the DLP LightCraft 4500. The Single-Chip Microcomputer is used to control the start or stop of the DLP and camera. The computer is used to reconstruct the 3-D surface of the object after the captured fringes processing. In addition, the synchronous signal is sent to the CCD through the external output of DLP, so as to realize the synchronization between them. The experimental process is described in Fig. 12.

5.1 Experimental Comparisons of Wrapped Phase Calculation Accuracy

The measured object is affected by the external sun light intensity, and the captured fringe image contain strong noise, as shown in Fig. 13(a). Since the anti-interference ability of the WRE-DMM is lower than that of other algorithms, WRE-ECF and WRE-ICF are adopted for comparisons. Meanwhile, Itoh phase unwrapping method is used for phase unwrapping. In 2-D WT, two-dimensional

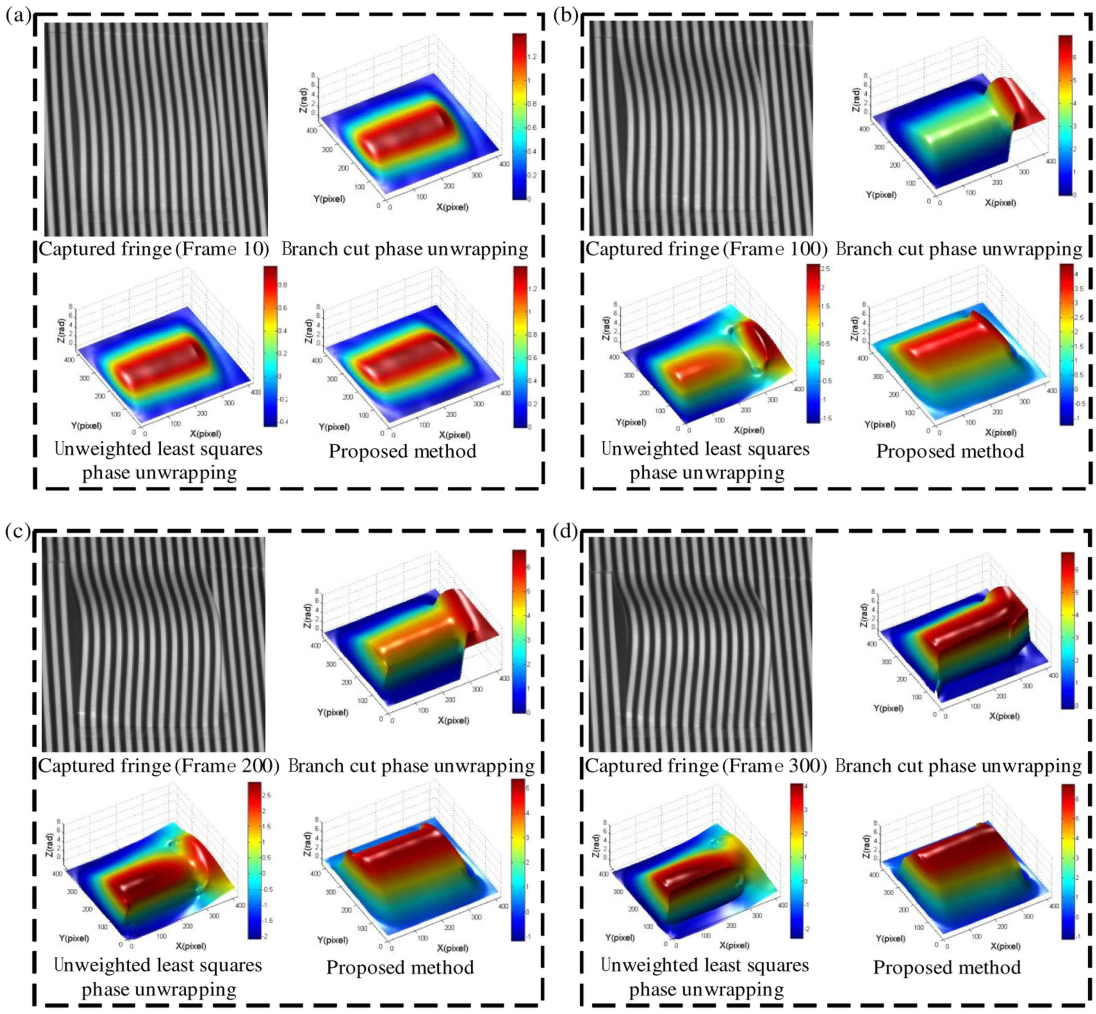

Fig. 14. 3-D reconstructed surfaces comparisons of dynamic convex surface. (a) Frame 10. (b) Frame 100. (c) Frame 200. (d) Frame 300. (Video 4: The captured fringe patterns video, Video 5: 3-D reconstructed shapes video based on WRE-ICF and unweighted least squares phase unwrapping, Video 6: 3-D reconstructed shapes video based on WRE-ICF and the 3-D FGQAB).

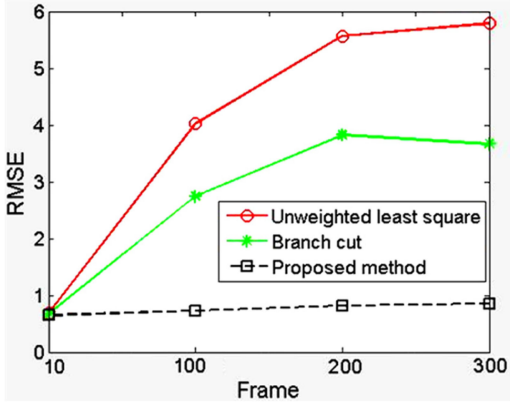

Fig. 15. RMSEs of continuously deformed objects at different moments.

TABLE 2
RMSEs Comparisons Between WRE-ECF and WRE-ICF

The measured object	WRE-ECF and Itoh	WRE-ICF and Itoh
Curved surface	1.0394	0.6851

Morlet mother wavelet is adopted. The parameters in 2-D WT are $k = 5.336$, $\theta = \{0, \pi/6, \pi/3, \pi/2\}$, $s = \{1, 2, \ldots, 64\}$. The values of a and b are consistent with the image size.

In addition, phase-shifting method has high accuracy and robustness in calculating the wrapped phase. However, phase-shifting method usually requires three or more fringes to calculate the wrapped phase, which is suitable for 3-D surface reconstruction of static objects. In this work, we take the phase calculated by the phase-shifting method and Itoh phase unwrapping as the ideal results. The reconstructed 3-D surfaces are shown in Fig. 13(b)–(d). The 3-D surfaces are cut to 300 pixels $\times$ 300 pixels for local comparison. From the comparison results, it can be seen that the 3-D surfaces using the WRE-ECF has some wrinkles, while the 3-D surfaces using the proposed method is smoother and closer to that using the phase-shifting method and Itoh phase unwrapping.

For quantitative comparisons, the 3-D measurement errors are evaluated by RMSE. The results are shown in Table 2. It can be seen that the RMSE of the 3D surface reconstructed by WRE-ICF and Itoh is 0.6851, which is reduced by 34.1% compared to the RMSE of the 3D surface reconstructed by WRE-ECF and Itoh.

5.2 Experimental Comparisons of Unwrapped Phase Calculation Accuracy

The measured object is a curved surface that continuously bulges over time. The wrapped phase is calculated by WRE-ICF. In the case that the wrapped phase is exactly the same, we compare the unwrapped phase using different phase unwrapping algorithms. Due to the large error of Itoh phase unwrapping, only the 3-D reconstruction of the branch cut phase unwrapping, least squares phase unwrapping and 3-D FGQAB proposed in this work are compared. In view of the space limitation of the article, four frames of fringe patterns and their 3-D reconstructed surfaces are shown in Fig. 14. When the height of the object changes drastically, the two-dimensional phase unwrapping methods (i.e., branch cut phase unwrapping, least squares phase unwrapping) will have larger errors, while the 3-D reconstructed surfaces based on the3-D FGQAB are better.

When the object is continuously deformed, the RMSEs of the 3-D reconstructed surfaces using different methods are shown in Fig. 15. The RMSEs of the 3D surfaces reconstructed by the 3-D FGQAB are much smaller than the RMSEs of other methods.

6. Conclusion

In this paper, a dynamic 3-D surface measurement method for continuously deformed objects is presented in detail. First, a 2-D WTP employing an improved cost function is adopted to obtain the wrapped phase. Then, a 3-D flood filling phase unwrapping algorithm guided by 3-D quality map avoiding 3-D branch cut is introduced to obtain the unwrapped phase. Our proposed method has the following advantages with respect to the other existing methods.

1) Only one fringe pattern is needed, so there is no need to consider the phase error between frames. Therefore, there is no need to consider the problem of inter frame error when capturing multiple fringes.
2) An improved 2-D WTP is introduced, which has higher anti-interference ability. Its phase calculation accuracy is higher than that of existing FTP and 2-D WTP.
3) A 3-D flood filling phase unwrapping algorithm guided by 3-D quality map avoiding 3-D branch cut is introduced to obtain the unwrapped phase. Compared with the two-dimensional phase unwrapping algorithm in a frame, the proposed 3-D phase unwrapping algorithm makes

full use of the relationship between the phases of each frame. Therefore, there are more unwrapping paths and the unwrapped phase error is limited to a smaller range.

The proposed method can be used for dynamic 3-D measurement of continuously deformed objects, such as impact, collision and other dynamic 3-D measurement, and has a wide range of application prospects.

References

[1] J. H. Wang, Y. G. Zhou, and Y. X. Yang, "Three-dimensional measurement method for nonuniform reflective objects," *IEEE Trans. Instrum. Meas.*, vol. 69, no. 11, pp. 9132–9143, Nov. 2020.

[2] J. H. Wang, Y. X. Yang, M. W. Shao, and Y. G. Zhou, "Three-dimensional measurement for rigid moving objects based on multi-fringe projection," *IEEE Photon. J.*, vol. 12, no. 4, Aug. 2020, Art. no. 6802114.

[3] S. J. Feng *et al.*, "Robust dynamic 3-D measurements with motion-compensated phase-shifting profilometry," *Opt. Lasers Eng.*, vol. 103, pp. 127–138, Apr. 2018.

[4] T. Y. Tao, Q. Chen, J. Da, S. J. Feng, Y. Hu, and C. Zuo, "Real-time 3-D shape measurement with composite phase-shifting fringes and multi-view system," *Opt. Exp.*, vol. 24, no. 18, pp. 20253–20269, Sep. 2016.

[5] W. Zhang, L. D. Yu, W. S. Li, H. J. Xia, H. X. Deng, and J. Zhang, "Black-box phase error compensation for digital phase-shifting profilomtry," *IEEE Trans. Instrum. Meas.*, vol. 66, no. 10, pp. 2755–2761, Oct. 2017.

[6] C. Zuo, S. J. Feng, L. Huang, T. Y. Tao, W. Yin, and Q. Chen, "Phase shifting algorithms for fringe projection profilometry: A review," *Opt. Lasers Eng.*, vol. 109, pp. 23–59, Oct. 2018.

[7] M. Takeda and K. Mutoh, "Fourier-transform profilometry for the automatic measurement of 3-D object shape," *Appl. Opt.*, vol. 22, no. 24, pp. 3977–3982, Jan. 1984.

[8] Z. B. Zhang and J. G. Zhong, "Applicability analysis of wavelet-transform profilometry," *Opt. Exp.*, vol. 21, no. 16, pp. 18777–18796, Aug. 2013.

[9] M. Zhong, F. Chen, C. Xiao, and Y. C. Wei, "3-D surface profilometry based on modulation measurement by applying wavelet transform method," *Opt. Lasers Eng.*, vol. 88, pp. 243–254, Jan. 2017.

[10] M. A. Gdeisata *et al.*, "Spatial and temporal carrier fringe pattern demodulation using the one-dimensional continuous wavelet transform: Recent progress, challenges, and suggested developments," *Opt. Lasers Eng.*, vol. 47, no. 12, pp. 1348–1361, Dec. 2009.

[11] Z. Y. Wang, J. Ma, and M. Vo, "Recent progress in two-dimensional continuous wavelet transform technique for fringe pattern analysis," *Opt. Lasers Eng.*, vol. 50, no. 8, pp. 1052–1058, Aug. 2012.

[12] J. M. Huntley and H. Saldner, "Error-reduction methods for shape measurement by temporal phase unwrapping," *J. Opt. Soc. Amer.*, vol. 14, no. 12, pp. 3188–3190, 1997.

[13] K. Itoh, "Analysis of the phase unwrapping algorithm," *Appl. Opt.*, vol. 21, no. 14, pp. 2470–2471, 1982.

[14] H. S. Abdul-Rahman, M. A. Gdeisat, D. R. Burton, M. J. Lalor, F. Lilley, and C. J. Moore, "Fast and robust Three-dimensional best path phase unwrapping algorithm" *Appl. Opt.*, vol. 46, no. 26, pp. 6623–6635, 2007.

[15] C. K. Yee and K. S. Yen, "Single frame profilometry with rapid phase demodulation on colour-coded fringes," *Opt. Commun.*, vol. 397, pp. 44–50, Aug. 2017.

[16] J. L. Flores, J. A. Ferrar, G. G. Torales, R. Legarda-saenz, and A. Silva, "Color-fringe pattern profilometry using a generalized phase-shifting algorithm," *Appl. Opt.*, vol. 54, no. 30, pp. 8827–8834, Oct. 2015.

[17] K. Liu, Y. C. Wang, D. L. Lau, Q. Hao, and L. G. Hassebrook, "Dual-frequency pattern scheme for high-speed 3-D shape measurement," *Opt. Exp.*, vol. 18, pp. 5229–5244, Mar. 2010.

[18] C. Zuo *et al.*, "High-speed three-dimensional shape measurement for dynamic scenes using bi-frequency tripolar pulse-width-modulation fringe projection," *Opt. Lasers Eng.*, vol. 51, no. 8, pp. 953–960, Mar. 2013.

[19] C. Zuo, Q. Chen, G. H. Gu, S. J. Feng, and F. C. Y. Feng, "High-speed three-dimensional profilometry for multiple objects with complex shapes," *Opt. Exp.*, vol. 20, pp. 19493–19510, Aug. 2012.

[20] C. Zuo, T. Y. Tao, S. J. Feng, L. Huang, A. Asundi, and Q. Chen, "PMicro Fourier transform profilometry (μFTP): 3D shape measurement at 10,000 frames per second," *Opt. Lasers Eng.*, vol. 102, pp. 70–91, Mar. 2018.

[21] J. Ma, Z. Y. Wang, and T. Y. Pan, "Two-dimensional continuous wavelet transform algorithm for phase extraction of two-step arbitrarily phase-shifted interferograms," *Opt. Lasers Eng.*, vol. 55, pp. 205–211, Apr. 2014.

[22] H. Niu, C. Quan, and C. Tay, "Phase retrieval of speckle fringe pattern with carriers using 2D wavelet transform," *Opt. Lasers Eng.*, vol. 47, no. 12, pp. 1334–1339, Apr. 2009.

[23] H. Liu, A. N. Cartwright, and C. Basaran, "Moiré interferogram phase extraction: A ridge detection algorithm for continuous wavelet transforms," *Appl. Opt.*, vol. 43, no. 4, pp. 850–857, Feb. 2004.

[24] A. Abid, "Fringe pattern demodulation using the one-dimensional continuous wavelet transform: Field-programmable gate array implementation," *Appl. Opt.*, vol. 52, no. 7, pp. 1468–1471, Mar. 2013.

[25] M. Zhong, F. Chen, C. Xiao, Y. Yang, and Y. C. Wei, "Noise reduction in modulation measurement profilometry based on the wavelet transform method," *Opt. Eng.*, vol. 57, no. 5, May 2018, Art. no. 054102.

[26] C. Jiang, S. H. Jia, J. Dong, Q. Lian, and D. C. Li, "Multi-frequency fringe projection profilometry based on wavelet transform," *Opt. Exp.*, vol. 24, no. 11, pp. 1323–1333, May 2016.

[27] J. C. Souza, M. E. Oliveira, and P. A. M. Santos, "Branch-cut algorithm for optical phase unwrapping," *Opt. Lett.*, vol. 40, no. 15, pp. 3456–3459, Aug. 2015.

[28] D. L. Zheng and F. P. Da, "A novel algorithm for branch cut phase unwrapping," *Opt. Lasers Eng.*, vol. 49, no. 5, pp. 609–617, May 2011.

[29] Y. Guo, X. T. Chen, and T. Zhang, "Robust phase unwrapping algorithm based on least squares," *Opt. Lasers Eng.*, vol. 63, pp. 25–29, Dec. 2014.